https://doi.org/10.1016/j.jcsr.2021.106817

Superior low-cycle fatigue performance of iron-based SMA for seismic damping application

Cheng Fang[1], Wei Wang[1]*, Yuezhen Ji[1], Michael CH Yam[2]

[1]State Key Laboratory of Disaster Reduction in Civil Engineering & Department of Structural Engineering, Tongji University, Shanghai 200092, China
[2]Department of Building & Real Estate, The Hong Kong Polytechnic University, Hung Hom, Kowloon, Hong Kong, China
** Corresponding author: email: weiwang@tongji.edu.cn, Tel: +86 (0)21-65982926*

Abstract: This study reveals the superior low-cycle fatigue performance of iron-based shape memory alloy (Fe-SMA) for seismic damping application, catering to the need for more durable, resilient, and perhaps fatigue-free structural systems in seismic active regions. The study commences with material tests examining both the macroscopic and microscopic properties of Fe-SMA under monotonic and cyclic loading, followed by calibration of combined hardening parameters to facilitate numerical modelling. A Fe-SMA shear damper specimen is tested, and its behavior is compared with its mild steel counterpart. Among other findings, the study revealed good ductility of Fe-SMA with a fracture strain of up to 55% under monotonic loading. The fatigue life of Fe-SMA is from 4007 to 83 when the strain amplitude increases from ±1% to ±9%, and the values could be 10 times that of common structural steel. The cyclic strain-life relationships of Fe-SMA can be readily presented by the conventional Basquin-Coffin-Manson relationship. Both kinematic and isotropic hardening characteristics of Fe-SMA are observed, and a combined kinematic/isotropic hardening model with calibrated parameters is shown to adequately capture the hysteretic behavior of the material. The subsequent damper tests provide further evidence of its superior fatigue performance, where a fatigue life of 173 cycles is observed for the Fe-SMA damper under a constant rotational angle of 4%, in contrast to 16 cycles for its normal steel counterpart. The unique phase transformation characteristic of Fe-SMA could also affect the fatigue failure mode, where different crack patterns are observed for the dampers with the different materials.

Keywords: Low-cycle fatigue; iron-based shape memory alloy (Fe-SMA); seismic; shear damper; combined kinematic/isotropic hardening.

1. Introduction

Low-cycle/extremely low-cycle fatigue (LCF/ELCF) is one of the main reasons for the damage of steel structures under earthquakes. The risk of failure is particularly high when the shaking is severe or the duration is long [1]. Many strong ground motions lasting for more than 60 seconds have been recorded during the 2008 Wenchuan, 2010 Chile, 2011 Tohoku and other major earthquakes, causing catastrophic damages to the structures [2-4]. It is also reminded that a main shock is often followed by a series of aftershocks. For example, the 2008 Wenchuan earthquake witnessed more than 40 aftershocks with Mw > 5.0; the main shock of the 2011 Tohoku earthquake was followed by 60 strong aftershocks with Mw > 6.0 [5]. Many aftershocks occur just within several days after the mainshock, rendering the opportunity of repairing the damaged members small (even if they are intended to be replaceable) in such short gaps.

Although significant progress has been made in understanding the fundamental seismic behavior of steel structures over the past decades, especially after the 1994 Northridge and 1995 Kobe earthquakes, failure is sometimes inevitable even in well-designed steel structures, mainly because of the ELCF [6-7]. In fact, the ELCF resistance of steel is mostly restricted by its inherent physical property, i.e., microvoid growth and subsequent coalescence, leading to the formation of final fracture surface [8]. Some steel members and dampers are designed to be replaceable, a concept which is theoretically feasible, but in practice the re-installation can be difficult due to the possible residual deformation and local damage to the connecting components [9-12]. There is a pressing need for more durable and resilient materials/structural systems which can minimize the damage and interruption after major earthquakes.

An emerging class of material called Fe-Mn-Si alloy provides a unique way to resolve the abovementioned issues. Fe-Mn-Si alloy is a class of iron-based shape memory alloy (Fe-SMA) which is well known for its shape-memory effect (SME) [13]. Apart from the SME, Fe-SMA also has excellent LCF/ELCF resistance, which is attributed to the diffusionless solid state phase transformation in which the atoms move in an organized manner relative to their neighbors, rather than the dislocation-based plasticity with irreversible slip exhibited by common structural steel [14]. Importantly, Fe-SMA is a low-cost material and can be massively produced with conventional metallurgical equipment such as electric arc furnace. This may make Fe-SMA more attractive than NiTi-based SMA (also known as NiTinol [15-23]), especially in the civil engineering sector. In addition, Fe-SMA has good corrosion-resistance due to the existence of Mn and Cr elements [24].

Practical applications of Fe-SMAs have first succeeded in crane rail and pipe industries [14]. The use of Fe-SMA for civil engineering structures has also been explored, where focus has been majorly on their SME property leading to prestressing capability. For example, EMPA (Swiss Federal Laboratories for Materials Science and Technology) has conducted extensive experimental investigations on concrete structures strengthened by Fe-SMA reinforcement [25-26]. Rojob and El-Hacha [27] also examined reinforced concrete beams strengthened with near-surface-mounted (NSM) Fe-SMA bars. In these studies, pre-deformed Fe-SMAs were embedded in the concrete and heated to 150~250 °C, and permanent prestress is induced after air cooling. The work was then extended to fatigue strengthening of steel plates and connections [28-31], where much increased fatigue life was realized.

While the SME of Fe-SMA has been widely studied, the potential for utilizing Fe-SMAs for durable seismic damping was not recognized until the completion of the JP Tower in Nagoya, Japan, 2015, the world's first project using Fe-SMA passive dampers. Tests done by the manufacturer suggested that the Fe-SMA shear dampers could have fatigue life more than 10 times that of their mild steel counterparts [14]. After the initial success, new classes of Fe-SMA with optimized chemical compositions have been developed by the community of material scientists to meet higher seismic protection demands [32-33], and the fatigue/cyclic behavior of Fe-SMA members has been studied [34-36]. Fe-SMA undoubtedly provides a new perspective for dealing with seismic-induced fatigue issues, and helps accelerate the development of next-generation fatigue-free and highly-resilient structural systems. However, the research is still in its early stage, and some essential problems are yet to be addressed. For example, most existing studies focused on the fatigue behavior of Fe-SMA at a small strain amplitude, e.g., ±1%, whereas a much larger strain is expected considering a strong earthquake event. The influence of strain amplitude on the fracture mechanism of Fe-SMA is not well understood, and the hysteretic law of the material and the associated modelling approach are insufficiently investigated. Furthermore, the fundamental behavior and failure mode of Fe-SMA dampers are inadequately examined. More studies are still in need before the new material can be confidently embraced by the construction industry.

This study aims to fill the knowledge gap by carrying out a comprehensive set of material-level tests to obtain the cyclic strain-life relationships and finite element (FE) modelling parameters for Fe-SMA. A total of 14 material tests are conducted, covering different materials (Fe-SMA and mild steel) and strain amplitudes (±1%~±9%). Cyclic plasticity parameters which are suitable for incorporating into FE models are then determined based on the material test results. Member-level study is subsequently carried out, where a specially designed Fe-SMA shear damper specimen is tested, and its behavior is compared with its mild steel counterpart.

2. Material test arrangements

The chemical composition of the material was Fe-17Mn-5Si-10Cr-5Ni (mass-%) alloy, which is a typical class of Fe-SMA exhibiting sound LCF/ELCF resistance. Fe-SMA cylindrical bars were produced for the material tests, where industrial pure iron (main impurities are C, Al, etc.), nickel, electrolytic manganese, silicon and electrolytic chromium were mixed according to the designed proportion. The raw materials were smelted in a vacuum mid-frequency induction furnace with a vacuum degree of 10^{-2} Torr. After dissolving the raw material, the high temperature was kept for 30 mins to make the composition uniform, and then the material was cast into 25 kg ingots. In order to set up homogenization microstructure, the ingot was annealed at 1200 °C for 24 h, and the oxide scale on the surface was removed. The ingot was then heated again to 1100 °C for 1 h, and hot forged into cylindrical bars (or flat plates for producing the shear damper, as discussed later). The cylindrical bar specimens were finished by turning and grinding, while the plate specimens were finished by wire cutting, annealing, straightening, and grinding. These specimens were finally subjected to solution heat treatment at 1000 °C for 1 h to mitigate the internal stress during the machining process. To facilitate comparison, specimens with grade Q235 (nominal f_y = 235 MPa) mild steel were also ordered and tested.

Both "long" and "short" cylindrical bar specimens were prepared, with the detailed dimensions given in Fig. 1(a). The former was for monotonic testing and the latter was for cyclic testing. The working length-to-diameter ratios of the bar specimens for monotonic and cyclic testing are 5.33 and 1.13, respectively. The dimensions of the working and transition segments were designed to make sure that buckling does not occur under the largest anticipated compressive strain, and that fracture is expected to occur inside the reduced working segment. Each test coupon was designated with a specimen code, starting with the material type, followed by type of loading, and, if applicable, ending with the strain amplitude or test number (for duplicate monotonic test). The details of the material test specimens are summarized in Table 1. The considered loading amplitudes can adequately cover both the LCF and ELCF regimes.

The material test specimens were gripped via friction by the hydraulic wedge jaws of an MTS Landmark 500kN Universal Test Machine (UTM), and tested under displacement (strain) control with a strain rate of $0.005s^{-1}$, as shown in Fig. 1(b). A series of MTS extensometers with gauge lengths from 10 mm to 30 mm were employed, catering to the different specimens. The tests terminated when the specimen fractured or the resisting load deteriorated to 50% of the maximum load (for fatigue testing). Both constant- and incremental-strain loading protocols were considered. The former employed a constant strain amplitude (ranging from ±1% to ±9%) until fracture of the specimen, and the latter started with a 1% initial strain and proceeded with a fixed strain incremental interval until final failure of the specimen (5 cycles were repeated at each strain amplitude).

3. Material test results and discussions

3.1 Monotonic test results

Three Fe-SMA cylindrical specimens were subjected to monotonic tensile testing, where the obtained engineering stress-strain curves, together with that of the Q235 steel, are shown in Fig. 2(a). The monotonic test results show that in contrast to the mild steel which typically exhibits a recognizable yield plateau prior to strain hardening, the Fe-SMA displays non-obvious yield point followed by substantial strain hardening. There is a clear demarcation between the initial linear stage (that below f_p) and the subsequent stage, which may be due to the initiation of martensitic transformation after reaching the proportional limit [13]. A summary of the basic material properties, i.e., Young's modulus (E), proportional limit (f_p), yield strength (i.e., 0.2% proof stress $f_{0.2\%}$), ultimate strength (f_u), and fracture strain (ε_u), of the Fe-SMA specimens, is given in Table 2. The material exhibits very good ductility with a fracture strain of up to 55%, and the fracture was accompanied by evident necking. The average f_u/f_y ratio is 2.72, indicating a significant reserve of the strength. It is noted that Fe-SMA elements should be more carefully designed in practice to avoid overstrength at the energy dissipation zone, and the existing design principle for steel dampers may be revisited. As further shown in Fig. 2(b), the rough fracture surface (according to visual observation) as well as the microscopic fractographic obtained by scanning election microscope (SEM) confirms the ductile fracture characteristic of the specimen under monotonic loading. The dimpled pattern, indicating a microvoid growth and coalescence fracture procedure, dominates the entire fracture surface.

3.2 Cyclic test results – basic hysteretic properties

The stress-strain curves of the material test specimens under cyclic loading are shown in Fig. 3, and Fig. 4 gives a further comparison of the half-life hysteretic behavior between the Fe-SMA and Q235 steel specimens. The hysteretic loops of the Fe-SMA are in general full and symmetric, and the hysteretic response is quickly stabilized from the second cycle. The shape of the loop is slightly "narrower" than that of the mild steel, with more significant hardening being observed. A slight nonlinear "spring-back phenomenon" is displayed during the unloading stage, as marked in Fig. 4. This behavior results from the minor superelasticity of the Fe-SMA at room temperature, although such effect is much less significant than that displayed by superelastic NiTi SMA, because of the coexisting irreversible plasticity of the Fe-SMA [14, 37]. The recovered strain due to superelasticity for the considered material is around 5~10% of the strain amplitude.

Moreover, Fe-SMA exhibits moderate cyclic hardening effect, as indicated by the cyclic stress-strain curves which are constructed by linking the tips of the stabilized loops at varying strain amplitudes as shown in Fig. 5(a). It is noted that the cyclic stress-strain curves can be established according to either constant strain amplitude tests (data from multiple specimens) or incremental strain amplitude tests (data from a single specimen) [7], where the latter was employed in this study. It is shown that the cyclic stress amplitude exceeds the corresponding stress from the monotonic tensile tests. At the maximum considered strain amplitude of 9%, the stress of the cyclic stress-strain curve is approximately 15% larger than the monotonic tensile test value.

The cyclic stress-strain curve could be described by Ramberg-Osgood models, as expressed by:

$$\frac{\Delta\varepsilon}{2} = \frac{\Delta\varepsilon_e}{2} + \frac{\Delta\varepsilon_p}{2} = \frac{\Delta\sigma}{2E} + \left(\frac{\Delta\sigma}{2K'}\right)^{\frac{1}{n'}} \tag{1}$$

where $\Delta\varepsilon_e/2$ and $\Delta\varepsilon_p/2$ are the elastic and plastic strain amplitudes, respectively; $\Delta\sigma/2$ is the stress amplitude which is obtained from the stabilized half-life hysteretic loop; K' and n' are the strength coefficient and cyclic strain hardening exponent, respectively, which are determined via curve fitting. The fitted values are: K' = 1483.80, and n' = 0.2701. The cyclic behavior of the material can be further examined by re-plotting the hysteretic loops at different strain amplitudes in the same figure, where the compressive peaks are superimposed at the same origin. If the ascending curves of these hysteresis loops coincide, the material is deemed to display a "Masing" property with kinematic hardening. It can be observed from Fig. 5(b) that Fe-SMA is not a typical Masing material, implying that the material may exhibit a combined kinematic and isotropic hardening behavior.

3.3 Fatigue properties

The fatigue life, i.e., the number of cycles to failure (N_f), of the Fe-SMA specimens obtained from the constant-strain amplitude tests is summarized in Table 3. The fatigue life of the Q235 mild steel examined in this study as well as the test data from other independent researchers [7, 38-40] are also given in the table for comparison. It is clearly shown that Fe-SMA displays superior fatigue life relative to common structural steels, including low-yield point (LYP) steel, stainless steel, and carbon steel. For example, the fatigue life of Fe-SMA is 5~10 times that of LYP steel, the latter is a popular class of seismic damping material due to its favorable low yield strength (which encourages early participation in energy dissipation) and good fatigue resistance.

As mentioned, the total strain amplitude $\Delta\varepsilon/2$ can be decomposed into elastic strain amplitude $\Delta\varepsilon_e/2$ and plastic strain amplitude $\Delta\varepsilon_p/2$. Previous studies showed that the plastic strain vs. fatigue life relationship of steel approximately follows a straight line when plotted on a log-log scale. This observation is popularly known as basic Coffin-Manson relationship [41-42], which is expressed as:

$$\frac{\Delta\varepsilon_p}{2} = \varepsilon_f^{'}\left(2N_f\right)^c \tag{2}$$

where ε_f' and c are fatigue ductility coefficient and fatigue ductility exponent, respectively, which can be obtained via curve fitting, and $2N_f$ is the number of reversals to failure, twice the number of cycles to failure. By taking the elastic strain amplitude into account, a Basquin-Coffin-Manson relationship can be established, as expressed as:

$$\frac{\Delta\varepsilon}{2} = \frac{\Delta\varepsilon_e}{2} + \frac{\Delta\varepsilon_p}{2} = \frac{\sigma_f^{'}}{E}\left(2N_f\right)^b + \varepsilon_f^{'}\left(2N_f\right)^c \tag{3}$$

where σ_f' and b are the fatigue strength coefficient and fatigue strength exponent, respectively. By fitting the experimental data, the Basquin-Coffin-Manson relationship is presented in Fig. 6(a), which suggests that the existing strain-fatigue life prediction model is also applicable to Fe-SMA. The figure also shows that the fatigue life is weakly correlated with the elastic strain amplitude, implying that their influence on the fatigue life is relatively insignificant. The transition fatigue life point (i.e., the demarcation between low-cycle and high-cycle fatigues), which is determined by the intersection between the fitted $\Delta\varepsilon_e/2$-N_f and $\Delta\varepsilon_p/2$-N_f lines, is approximately at $2N_f = 93638$, and the corresponding total strain amplitude $\Delta\varepsilon/2$ is ±0.2%. This again confirms that the ±1% to ±9% strain amplitude considered in this study leads to fatigue behavior dominated by LCF or ELCF in contrast to high cycle fatigue (HCF). By placing the strain-fatigue life data of Fe-SMA and the data of other different types of structural steel together in Fig. 6(b), the superior low-cycle fatigue performance of Fe-SMA is highlighted.

3.4 Microscopic fractography from cyclic tests

To better understand the fracture mechanism of the Fe-SMA under the considered cyclic loading, the macroscopic visual observation of the entire fractured section, as well as the microscopic fractographic observation of the fracture surfaces characterized by SEM, are further provided in Figs. 7 and 8, respectively. Two strain amplitudes, ±1% and ±9%, are selected as representative cases. As shown in Fig. 7, a visible boundary between the fatigue crack growth (FCG) region and the final fracture (FF) region is seen. The former (light region) is characterized by a smooth brittle fracture surface, and the latter (darker region) is characterized by pronounced surface roughening with ductile deformation features (dimples). As anticipated, an increase in the strain amplitude leads to limited fatigue crack propagation and hence a larger area of the FF region, showing that the fracture is more governed by the ductile quasi-static tensile behavior.

Fig. 8(a) shows the typical SEM fractograph at the FF region of the ±1% strain amplitude test specimen (location #1 in Fig. 7). The fracture surface is dominated by dimpled patterns, indicating a ductile microvoid growth and coalescence fracture procedure. On the other hand, Fig. 8(b) shows the SEM fractograph at the edge of the fatigue crack growth region (location #2 in Fig. 7). As anticipated, extensive developments and propagations of fatigue cracks were observed, confirming that fatigue fracture is originated from this region. Fig. 8(c) is the SEM fractograph selected from the boundary between the FCG and the FF regions (location #3 in Fig. 7), and Fig. 8(d) takes a close look at the FCG region, where river and terrace patterns, indicating brittle cleavage behavior, are observed. Insignificant but recognizable dimpled fracture patterns can also be seen in some local areas, which implies that the brittle fracture is preceded by minor plastic dissipation. Nevertheless, the overall ductility of the FCG region is very limited.

The main features of the SEM fractographs for the ±9% strain amplitude test specimen are similar to those for the ±1% strain amplitude test specimen, although some extra observations are worth mentioning. Fig. 8(e) shows the edge of the FF region (location #4 in Fig. 7), where a demarcation is found which is due to the existence of the macroscopic shear lip. The region above the boundary line (the shear lip region) in Fig. 8(e) displays shear-type dimples, where the region below the boundary line (normal FF region) has dimple patterns similar to those shown in Fig. 8(a). The cup-and-cone fracture morphology is because the high strain amplitude cyclic loading tends to result in material behavior being more similar to that under the monotonic tensile test (typically with necking and hence cup-and-cone fracture morphology prior to fracture). Finally, Fig. 8(f) shows the boundary between the FCG and FF regions (location #5 in Fig. 7), which again confirms the evolution from brittle to ductile fracture characteristics along the propagation of the fatigue crack.

3.5 Energy dissipation

The energy dissipation capability of the specimens can be presented by either the absolute energy dissipation per cycle W_D or a dimensionless index, i.e., equivalent viscous damping ratio (EVD), as defined by:

$$EVD = \frac{W_D}{4\pi W_E} \tag{4}$$

where W_D is essentially the area enclosed by the considered hysteretic loop, and W_E is the strain energy stored in a corresponding linear system. The EVDs of the specimens obtained from the half-life cycle are remarked in Fig. 3. It can be seen that the EVD of the Fe-SMA specimens ranges between 0.37 and 0.47, depending on the strain amplitude, and the value is on average 20% lower than that of the Q235 steel. This is because the EVD is only related to the shape of the hysteretic curve, where more significant strain hardening of the Fe-SMA causes increased W_E and hence decreased EVD. On the other hand, the absolute energy dissipation per cycle W_D of the Fe-SMA is slightly larger than that of the Q235 steel.

4. Finite element simulation

The current test results suggest that Fe-SMA could exhibit both kinematic and isotropic hardening characteristics under cyclic loading, and therefore it is anticipated that a combined kinematic/isotropic hardening model may adequately capture its fundamental hysteretic behavior. In order to facilitate the numerical simulation of Fe-SMA components, the key parameters for a commonly used constitutive model for cyclic plasticity of metals, i.e., "combined hardening model" in the nonlinear finite element software ABAQUS [43], is calibrated in this study. This model is based on the theory proposed by Chaboche [44]; it involves a kinematic hardening component and an isotropic hardening component, and hence is capable of describing both translation and uniform expansion of the yield surface in the stress space.

The parameters for the kinematic hardening component that accounts for the Bauschinger effect are calibrated through a stabilized cycle, e.g., a half-life cycle, as shown in Fig. 9(a). The stress-strain loop is first converted to the stress-plastic strain loop by subtracting the corresponding elastic strain, $\varepsilon = \sigma/E$. A series of (σ_i, ε_i^{pl}) data pairs are obtained considering the following coordinate translation rule:

$$\varepsilon_i^{pl} = \varepsilon_i - \frac{\sigma_i}{E} - \varepsilon_p^0 \quad (5)$$

where ε_p^0 is the value of the smallest plastic strain at zero stress, as marked in Fig. 9(a). For each data pair, the corresponding backstress is obtained from:

$$\alpha_i = \sigma_i - \frac{\sigma_1 + \sigma_n}{2} \quad (6)$$

where σ_1 and σ_n are the stresses in the first and last data pairs, respectively. The obtained (α_i, ε_i^{pl}) data pairs are used for obtaining the necessary kinemetric hardening parameters, given the following equation that defines the backstress:

$$\alpha = \sum_{k=1}^{n} \frac{C_k}{\gamma_k}\left(1 - e^{-\gamma_k \varepsilon^p}\right) \tag{7}$$

in which C and γ are the constants needing to be calibrated. In particular, the C/γ ratio defines the maximum change in the backstress and γ describes the rate at which the backstress changes with plastic strain. In some cases, considering only one set of backstress could not well capture the nonlinear kinematic hardening behavior, and as recommended by the ABAQUS manual [43], several kinematic hardening components (backstresses) can be superposed, which may effectively improve the simulation results.

For the isotropic hardening component, Chaboche [44] assumes that the change of the size of the yield surface depends on the equivalent plastic strain $\varepsilon^{p,acc}$, as expressed as:

$$\sigma = \sigma|_0 + Q_\infty\left(1 - e^{-b_{iso}\varepsilon^{p,acc}}\right) \tag{8}$$

where $\sigma|_0$ is the yield stress without experiencing any plastic strain, i.e., yield stress at $\varepsilon^{p,acc} = 0$, Q_∞ is the isotropic hardening constant which describes the maximum change in the size of the yield surface, and b_{iso} is the isotropic hardening exponent defining the rate of the change of the yield surface size with increasing plastic strain. The two constants Q_∞ and b_{iso} need to be calibrated through (σ_i, $\varepsilon_i^{p,acc}$) data pairs, where σ_i is the size of the yield surface in the i^{th} cycle, as obtained from:

$$\sigma_i = \frac{\sigma_i^t - \sigma_i^c}{2} \tag{9}$$

where σ_i^t and σ_i^c are the maximum tensile and compressive stresses of the i^{th} cycle, as shown in Fig. 9(b). The corresponding $\varepsilon_i^{p,acc}$ is expressed as:

$$\varepsilon_i^{p,acc} = \frac{1}{2}(4i - 3)\Delta\varepsilon_p \tag{10}$$

in which $\Delta\varepsilon_p$ is the plastic strain range as marked in the figure.

The material model parameters calibrated for each test specimen are summarized in Table 4, and typical stress-strain relationships predicted by the numerical model employing the considered parameters are shown in Fig. 10. It is worth mentioning that two sets of backstress are included in the kinematic hardening component in order to better capture the minor nonlinear "spring-back phenomenon", a unique property exhibited by Fe-SMA, in the unloading branch. In addition, $\gamma_2 = 0$ means that one of backstresses is expressed by a linear relationship, i.e., Eq. (7) is automatically changed to Eq. (11) in ABAQUS.

$$\alpha = \frac{C_1}{\gamma_1}\left(1 - e^{-\gamma_1 \varepsilon^p}\right) + C_2 \varepsilon^p \tag{11}$$

It is also noted that some model parameters vary with different specimens (i.e., with different strain amplitudes). This is in fact a very common case for metals [6-7, 45] because the evolving hysteretic shapes need to be captured by different combinations of the isotropic and kinematic components and their associated parameters. In practice, engineers may choose an appropriate set of calibrated parameters by assessing the anticipated working strain range of the material; alternatively, average values may be adopted.

5. Fe-SMA shear damper

5.1 Test arrangement

Following the material-level investigation, this section sheds further light on the potential of Fe-SMA for seismic damping applications. Two 6 mm-thick shear damper specimens with an identical shape were produced, as shown in Fig. 11, where one was made of Fe-SMA and the other was made of Q235 steel ordered from the same supplier who provided the material test coupons. The reduced width at mid height with an arc geometric transition was designed to alleviate stress concentration. The chemical composition of the Fe-SMA for the shear damper was the same as that adopted for the material test specimens. The shear damper was connected to the upper and lower angles via a series of Grade 10.9 M24 slip-critical high-strength bolts, and these angles were then connected to the test frame. A set of stiffened buckling-restraining plates (BRPs) was used to prevent out-of-plane deformation of the damper plate, while allowing free in-plane shear deformation. There was no intended gap between the damper plate and the BRPs, while a certain amount of grease was applied between the plates to reduce the friction. Both the angles and the BRPs are made of Q345 steel with nominal f_y = 345 MPa, and these components were oversized to ensure that they remained elastic and behaved almost in a rigid fashion.

The details of the test setup are shown in Fig. 12. The tests were carried out in the Structural Engineering Lab at Tongji University. The testing system included a 1500 kN electro-hydraulic servo actuator, a shear loading frame (including a horizontal loading beam) and a base. The actuator and the loading beam were connected via a hinge connection, and four more hinge connections were adopted for the shear loading frame to facilitate the shear deformation of the damper. Fig. 12 also shows the arrangement of the instrumentation. Four horizontal displacement transducers were used to measure the relative horizontal displacement of the top and bottom angles, where the average value was used as the shear displacement. Such an arrangement could also facilitate the detection of possible torsion of the damper during the test. Two more vertical displacement transducers were used to measure the vertical deformation (if any) of the damper. A fatigue loading protocol was employed, where a constant shear displacement amplitude of ±6 mm, corresponding to a ±4% rotational angle (6 mm divided by 150 mm), was applied until failure of the damper specimen. This rotational angle is expected to represent a moderate level of deformation demand for the considered shear dampers where the maximum equivalent strain is around 3%, according to numerical simulation (as explained later). This is a reasonable and practical peak strain level expected for a metal damper under design earthquakes.

5.2 Test results and discussions

The shear resistance vs. displacement responses of the damper specimens are shown in Fig. 13. Both dampers showed stable hysteretic performance. Due to the partial superelasticity, the shape of the hysteretic curve of the Fe-SMA damper is slightly narrower than that of its steel counterpart, a phenomenon which is consistent with the material test results. The thinner hysteretic shape of the Fe-SMA damper, on one hand, indicates smaller energy dissipation (EVD = 0.34 vs. 0.45 at half-life cycle), but on the other hand, may be effective in reducing the residual deformation of the structure. More encouragingly, the fatigue life (i.e., the number of cycles when the maximum shear resistance degraded to 85% of the peak value) of the Fe-SMA damper reached 173 cycles, which is more than 10 times that of the steel damper. This provides strong test evidence of the superior low-cycle fatigue performance of Fe-SMA for seismic damping application.

The BRPs were removed for a detailed inspection of the damaged damper plate after each test. It is of interest to find that the two damper specimens exhibited different crack patterns. As shown in Fig. 14, the Fe-SMA damper exhibited vertical cracks in the center of the plate, whereas the cracks of the steel damper were initiated from the edge of the plate. This difference confirms that Fe-SMA has unique plastic deformation and fracture mechanisms, and suggests that the microvoid growth and coalescence process of the material may be affected by the solid state phase transformation [13]. In addition, the way that stress triaxiality affects the micro-fatigue behavior of Fe-SMA might be different from normal steel. Further research opportunity exists to reveal how the microscopic feature of Fe-SMA would affect the macroscopic fatigue failure mode of the dampers, although this is beyond the scope of the present study.

5.3 Numerical simulation

Before moving on to the conclusion part, the calibrated combined hardening material parameters are adopted here to simulate the hysteretic behavior of the Fe-SMA shear damper. The finite element analysis (in ABAQUS) was carried out with the following two main objectives: 1) to show the applicability of the combined hardening material model to typical Fe-SMA components which are subjected to more complex stress/strain fields, and 2) to further interpret the load carrying mechanism of the dampers, and especially to reveal the stress distributions over the plate, information which is difficult to fully obtain from the test. Solid elements were used to model the damper plate as well as the adjacent components. To facilitate convergence, the buckling restrained status of the damper plate was approximately simulated by intentionally discarding the geometric nonlinearity option during the analysis, such that no shear buckling (out-of-plane deformation) is developed while the necessary stress field is adequately captured. Bolt preload was considered, and the contact between the damper plate and the angle legs was simulated by defining a hard contact behavior with Coulomb friction. Due to the lack of data, the friction coefficient was provisionally assumed to be 0.3 for general cleaned surfaces [46]. The damper model and the meshing scheme are shown in Fig. 15.

Considering that the maximum strain of the damper under 4% rotational angle is approximately 3%, the calibrated combined hardening material parameters obtained from the ±3% strain amplitude material test were employed for the damper model. For the remaining components which essentially remain elastic, a simple bilinear kinematic hardening material model was adopted. Fig. 15 shows the predicted hysteretic curve and the typical von Mises stress and equivalent plastic strain (PEEQ) distributions of the Fe-SMA damper at the maximum deformation. It is observed that the arc edge of the damper plate exhibits the highest stress/strain demand, and therefore this region is more prone to fatigue crack. The central region also exhibits large inelastic strains. As crack propagation could be very slow for the Fe-SMA damper, it is possible that the central region experienced cracking prior to an obvious formation of the crack at the arc edge. The unique crack propagation mechanism, together with other possible reasons discussed above, attributes to the difference in the failure mode between the Fe-SMA and steel dampers.

6. Summary and conclusions

This study has discussed the potential of Fe-SMA for seismic damping application, especially for the cases of high fatigue resistance demand. Material tests were first conducted to obtain the basic material properties and fatigue resistance, with discussions aided by microscopic characteristics obtained from SEM. Combined hardening parameters for Fe-SMA were also developed to facilitate FE modelling of the material. A Fe-SMA shear damper specimen was subsequently tested, and its behavior was compared with a steel damper. The main conclusions and comments are summarized as follows.

- Fe-SMA exhibits a non-obvious yield plateau prior to substantial strain hardening under monotonic loading. The material has very good ductility with a fracture strain of up to 55%, where the fracture was accompanied by evident necking. The entire fracture surface is dominated by dimpled pattern, reaffirming a ductile fracture procedure.

- The hysteretic loops of the Fe-SMA are full, stable and symmetric, although being slightly narrower than those of mild steel due to the superelasticity-induced spring-back phenomenon displayed during the unloading stage. The hysteretic response is stabilized and almost saturated from the second cycle. The cyclic stress exceeds the corresponding stress from the monotonic tensile tests, indicating a cyclic hardening effect.
- The fracture surface of Fe-SMA coupons under cyclic loading consists of a fatigue crack growth (FCG) region characterized by a smooth brittle fracture surface and a final fracture (FF) region characterized by pronounced surface roughening with ductile deformation features. An increase in the strain amplitude leads to limited fatigue crack propagation and hence a larger area of the FF region, and the fracture is more governed by ductile quasi-static tensile behavior.
- Fe-SMA displays fatigue lives far superior to common structural steels. The number of cycles to failure for Fe-SMA is from 4007 to 83 when the strain amplitude changes from ±1% to ±9%, while the values for the Q235 steel are from 578 to 15 under the same considered strain amplitudes. By comparisons against the other independent studies, Fe-SMA could have LCF/ELCF life 10 times that of common structural steel. The cyclic strain-life relationships of Fe-SMA can be readily presented by the Basquin-Coffin-Manson relationship.
- Fe-SMA exhibits both kinematic and isotropic hardening characteristics under cyclic loading, and a combined kinematic/isotropic hardening model is shown to adequately capture its fundamental hysteretic behavior. The key parameters for the “combined hardening model” in the nonlinear finite element software ABAQUS have been calibrated for engineering use.
- Test evidence of the superior fatigue performance of Fe-SMA was further provided by observing a fatigue life of 173 cycles for the Fe-SMA shear damper under a constant rotational angle of ±4%, whereas the fatigue life for its steel counterpart was only 16. The Fe-SMA damper exhibited vertical cracks in the center of the plate, whereas the cracks of the steel

damper were initiated from the edge of the plate. This difference suggests unique plastic deformation and fracture mechanisms of Fe-SMA which are worth future investigations.

7. Acknowledgement

The financial supports from the National Natural Science Foundation of China (NSFC) with Grant Nos. 51778456, 52078359, 51820105013 and 51778459 are gratefully acknowledged. Support for this study was also provided by the Shanghai Rising-Star Program (20QA1409400).

8. References

[1] Hou H, Qu B. Duration effect of spectrally matched ground motions on seismic demands of elastic perfectly plastic SDOFS. Engineering Structures, 2015, 90: 48-60.

[2] Bravo-Haro M A, Elghazouli A Y. Influence of earthquake duration on the response of steel moment frames. Soil Dynamics and Earthquake Engineering, 2018, 115: 634-651.

[3] Raghunandan M, Liel A B. Effect of ground motion duration on earthquake-induced structural collapse. Structural Safety, 2013, 41: 119-133.

[4] Marsh, M. L., & Gianotti, C. M. (1994). Structural response to long-duration earthquakes. Report No. WA-RD 340.1, Washington State Department of Transportation.

[5] Paterson E, Re D D, Wang Z. The 2008 Wenchuan earthquake: risk management lessons and implications. Risk Management Solutions, Inc, 2008. Newark, CA 94560.

[6] Narendra P V R, Prasad K, Krishna E H, et al. Low-Cycle-Fatigue (LCF) behavior and cyclic plasticity modeling of E250A mild steel. Structures, 2019, 20: 594-606.

[7] Nip K H, Gardner L, Davies C M, et al. Extremely low cycle fatigue tests on structural carbon steel and stainless steel. Journal of constructional steel research, 2010, 66(1): 96-110.

[8] Kanvinde A. Predicting fracture in civil engineering steel structures: State of the art. Journal of Structural Engineering, 2017, 143(3): 03116001.

[9] McCormick J, Aburano H, Ikenaga M, Nakashima M. Permissible residual deformation levels for building structures considering both safety and human elements. Proc. 14th World Conf. Earthquake Engineering, Seismological Press of China, Beijing, 2008.

[10] Fang C, Zhong Q, Wang W, Hu S, Qiu C. Peak and residual responses of steel moment-resisting and braced frames under pulse-like near-fault earthquakes. Engineering Structures 2018; 177: 579-597.

[11] Erochko J, Christopoulos C, Tremblay R, Choi H. Residual drift response of SMRFs and BRB frames in steel buildings designed according to ASCE 7-05. Journal of Structural Engineering, 2011, 137(5): 589-599.

[12] Esteva L. The Mexico earthquake of September 19, 1985—Consequences, lessons, and impact on research and practice. Earthquake Spectra, 1988, 4(3): 413-426.

[13] Cladera A, Weber B, Leinenbach C, et al. Iron-based shape memory alloys for civil engineering structures: An overview. Construction and building materials, 2014, 63: 281-293.

[14] Sawaguchi T, Maruyama T, Otsuka H, et al. Design concept and applications of Fe–Mn–Si-based alloys—from shape-memory to seismic response control. Materials Transactions, 2016, 57(3): 283-293.

[15] Fang C, Yam MCH, Lam ACC, Xie LK. Cyclic performance of extended end-plate connections equipped with shape memory alloy bolts. Journal of Constructional Steel Research 2014; 94(94):122-36.

[16] Yam MCH, Fang C, Lam ACC, Zhang YY. Numerical study and practical design of beam-to-column connections with shape memory alloys. Journal of Constructional Steel Research 2015; 104:177-92.

[17] Wang B, Zhu S, Qiu C, Jin H. High-performance self-centering steel columns with shape memory alloy bolts: Design procedure and experimental evaluation. Engineering Structures 2019; 182: 446-458.

[18] Wang W, Fang C, Liu J. Self-centering beam-to-column connections with combined superelastic SMA bolts and steel angles. Journal of Structural Engineering 2017, 04016175.

[19] Fang C, Wang W, He C, Chen YY. Self-centring behavior of steel and steel-concrete composite connections equipped with NiTi SMA bolts. Engineering Structures 2017;150:390-408.

[20] Wang W, Fang C, Yang X, Chen YY, Ricles J, Sause R. Innovative use of a shape memory alloy ring spring system for self-centering connections. Engineering Structures 2017;153:503-15.

[21] Qiu C, Zhu S. Shake table test and numerical study of self-centering steel frame with SMA braces. Earthquake Engineering & Structural Dynamic 2017;46(1):117-37.

[22] Fang C, Yam MCH, Ma HW, Chung KF. Tests on superelastic Ni–Ti SMA bars under cyclic tension and direct-shear: towards practical recentring connections. Materials and Structures 2015;48(4):1013-30.

[23] Wang W, Fang C, Liu J. Large size superelastic SMA bars: heat treatment strategy, mechanical property and seismic application. Smart Materials and Structures 2016;25(7):075001.

[24] Nishimura T. Nano Structure of the Rust Formed on an Iron-based Shape Memory Alloy (Fe–Mn–Si–Cr) in a High Chloride Environment. ISIJ International, 2014, 54(8): 1913-1919.

[25] Czaderski C, Shahverdi M, Brönnimann R, et al. Feasibility of iron-based shape memory alloy strips for prestressed strengthening of concrete structures. Construction and Building Materials, 2014, 56: 94-105.

[26] Shahverdi M, Czaderski C, Annen P, et al. Strengthening of RC beams by iron-based shape memory alloy bars embedded in a shotcrete layer. Engineering Structures, 2016, 117: 263-273.

[27] Rojob H, El-Hacha R. Self-prestressing using iron-based shape memory alloy for flexural strengthening of reinforced concrete beams. ACI Structural Journal, 2017, 114(2): 523-532.

[28] Izadi M, Motavalli M, Ghafoori E. Iron-based shape memory alloy (Fe-SMA) for fatigue strengthening of cracked steel bridge connections. Construction and Building Materials, 2019, 227: 116800.

[29] Hosseini A, Michels J, Izadi M, et al. A comparative study between Fe-SMA and CFRP reinforcements for prestressed strengthening of metallic structures. Construction and Building Materials, 2019, 226: 976-992.

[30] Ghafoori E, Neuenschwander M, Shahverdi M, et al. Elevated temperature behavior of an iron-based shape memory alloy used for prestressed strengthening of civil structures. Construction and Building Materials, 2019, 211: 437-452.

[31] Izadi M R, Ghafoori E, Motavalli M, et al. Iron-based shape memory alloy for the fatigue strengthening of cracked steel plates: Effects of re-activations and loading frequencies. Engineering Structures, 2018, 176: 953-967.

[32] Sawaguchi T, Nikulin I, Ogawa K, et al. Designing Fe–Mn–Si alloys with improved low-cycle fatigue lives. Scripta Materialia, 2015, 99: 49-52.

[33] Yoshinaka F, Sawaguchi T, Ilya N, et al. Improved fatigue life of the newly developed Fe-15Mn-10Cr-8Ni-4Si seismic damping alloy. Procedia Structural Integrity, 2019, 19: 214-223.

[34] Rosa D I H, Hartloper A, e Sousa A C, et al. Experimental behavior of iron-based shape memory alloys under cyclic loading histories. Construction and Building Materials, 2021, 272: 121712.

[35] Hosseini E, Ghafoori E, Leinenbach C, et al. (2018). Stress recovery and cyclic behaviour of an Fe–Mn–Si shape memory alloy after multiple thermal activation. Smart Materials and Structures,27(2), 025009.

[36] Ghafoori E, Hosseini E, Leinenbach C, et al. (2017). Fatigue behavior of a Fe-Mn-Si shape memory alloy used for prestressed strengthening. Materials & Design, 133, 349-362.

[37] Sawaguchi T, Kikuchi T, Kajiwara S. The pseudoelastic behavior of Fe–Mn–Si-based shape memory alloys containing Nb and C. Smart materials and structures, 2005, 14(5): S317.

[38] Shi G, Gao Y, Wang X, Zhang Y. Low cycle fatigue properties of low yield point steels. China Civil Engineering Journal. 2019,52(01):20-26+52 (In Chinese).

[39] Ge RR, Xue YT, Niu XY. Experimental study on low-cycle fatigue behavior of Chinese LYP225. China Civil Engineering Journal. 2017(01):16-23+49 (In Chinese).

[40] Dusicka P, Itani A M, Buckle I G. Cyclic response of plate steels under large inelastic strains. Journal of Constructional Steel Research, 2007, 63(2): 156-164.

[41] Coffin Jr LF. A study of the effects of cyclic thermal stresses on a ductile metal. Transactions of ASME 1954;76:931-50.

[42] Manson SS. Behavior of materials under conditions of thermal stress. National Advisory Commission on Aeronautics: Report 1170. Cleveland: Lewis Flight Propulsion Laboratory; 1954.

[43] ABAQUS. Analysis User's manual, v6.12, Dassault Systems Simulia Corp., Providence, USA, 2012.

[44] Chaboche JL. Time independent constitutive theories for cyclic plasticity. International Journal of Plasticity 1986;2(2):149-88.

[45] Yin F, Yang L, Wang M, Zong L, Chang X. Study on ultra-low cycle fatigue behavior of austenitic stainless steel. Thin-Walled Structures, 2019, 143: 106205.

[46] EN 1090-2:2018, Execution of steel structures and aluminium structures-technical requirements for steel structures, European Committee for Standardization, Brussels, Belgium, 2018.

Table 1 Summary of parameters for material test specimens

Test code	Material	Loading type	Strain amplitude
SMA-M-1	SMA	Monotonic	-
SMA-M-2	SMA	Monotonic	-
SMA-M-3	SMA	Monotonic	-
SMA-F-1%	SMA	Fatigue	±1%
SMA-F-3%	SMA	Fatigue	±3%
SMA-F-5%	SMA	Fatigue	±5%
SMA-F-7%	SMA	Fatigue	±7%
SMA-F-9%	SMA	Fatigue	±9%
SMA-I	SMA	Incremental	-
Q235-F-1%	Q235	Fatigue	±1%
Q235-F-3%	Q235	Fatigue	±3%
Q235-F-5%	Q235	Fatigue	±5%
Q235-F-7%	Q235	Fatigue	±7%
Q235-F-9%	Q235	Fatigue	±9%

Table 2 Basic material properties of Fe-SMA

Test	Young's modulus E (GPa)	Proportional limit f_p (MPa)	0.02% proof stress $f_{0.02\%}$ (MPa)	0.2% proof stress $f_{0.2\%}$ (MPa)	Ultimate strength f_u (MPa)	Fracture strain ε_u
SMA-M-1	182.08	125.49	205.86	261.96	747.46	0.5868
SMA-M-2	170.08	115.55	209.49	317.90	779.99	0.3507
SMA-M-3	164.05	106.26	200.08	313.54	768.50	0.5042
Average	172.07	115.77	205.14	297.8	774.25	0.4805

Table 3 Summary of fatigue life for different materials

Material	Strain amplitude				
	±1%	±3%	±5%	±7%	±9%
Fe-SMA (present work)	**4007**	**880**	**334**	**102**	**83**
Q235 (present work)	578	122	35	19	15
S355[7]	495~732	53~107	22~24	9~15	-
S235[7]	439~521	16~21	8~20	3	-
Stainless steel[7]	266~335	27~78	7~61	2~4	-
LYP100[38]	512~694	82~103	-	-	-
LYP100[38]	1008	121	40	-	-
LYP225[38]	1220	101	46	-	-
LYP225[39]	459~928	16~118	5~31	17	-
GR345[40]	536	69	27	16	-
HPS485[40]	400	51	21	13	-
HS440[40]	720	69	31	15	-
LYP225[40]	-	38	-	9	-
LYP100[40]	720	50	32	11	

Table 4 Calibrated material model parameters

Test	$\sigma\|_0$	C_1	γ_1	C_2	γ_2	Q_∞	b_{iso}
SMA-F-1%	170	32208.98	92.27	1788.8	0	60	3.5
SMA-F-3%	135	15222.35	60.99	1788.8	0	140	3
SMA-F-5%	80	26538.98	78.71	1788.8	0	140	3.5
SMA-F-7%	50	37081.41	81.99	1788.8	0	150	3.5
SMA-F-9%	35	36942.95	93.80	1788.8	0	180	3.5
Average	94	29598.934	81.55	1788.8	0	134	3.4

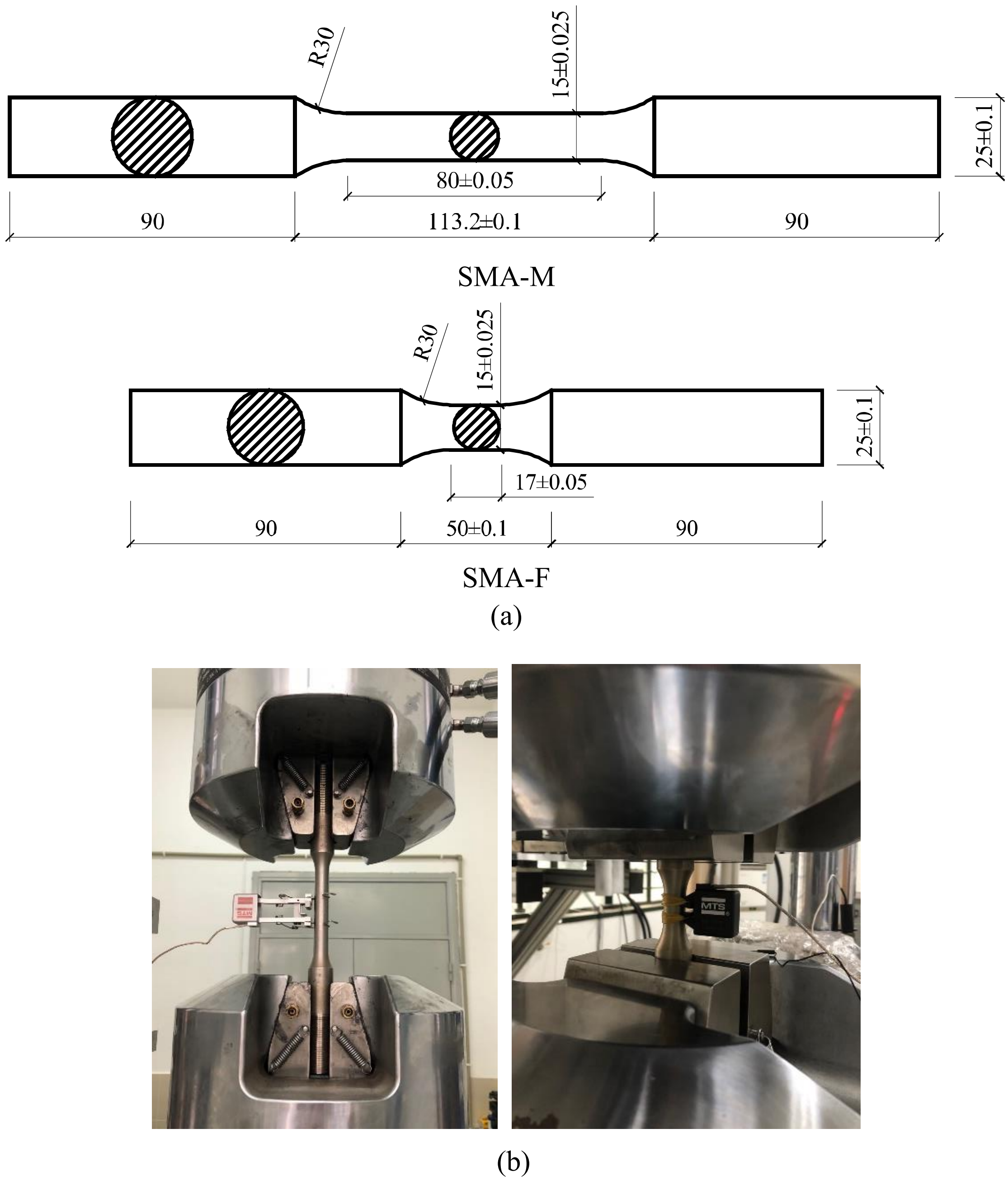

Fig. 1 Fe-SMA material tests: a) dimensions of material test specimens, b) test setup

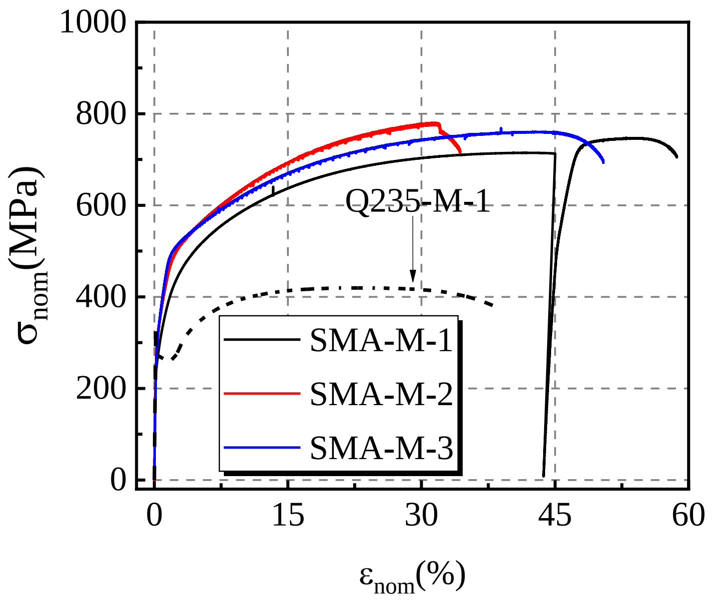

(a)

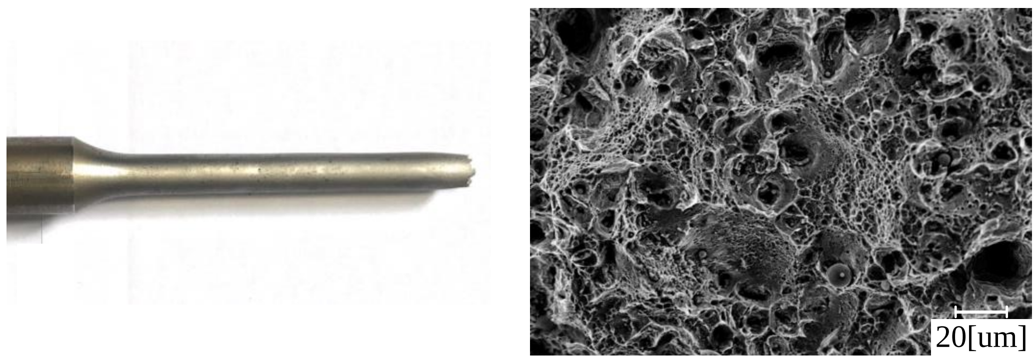

(b)

Fig. 2 Behavior of Fe-SMA under monotonic loading: a) stress-strain relationship, b) macroscopic fracture behavior and fractography by SEM

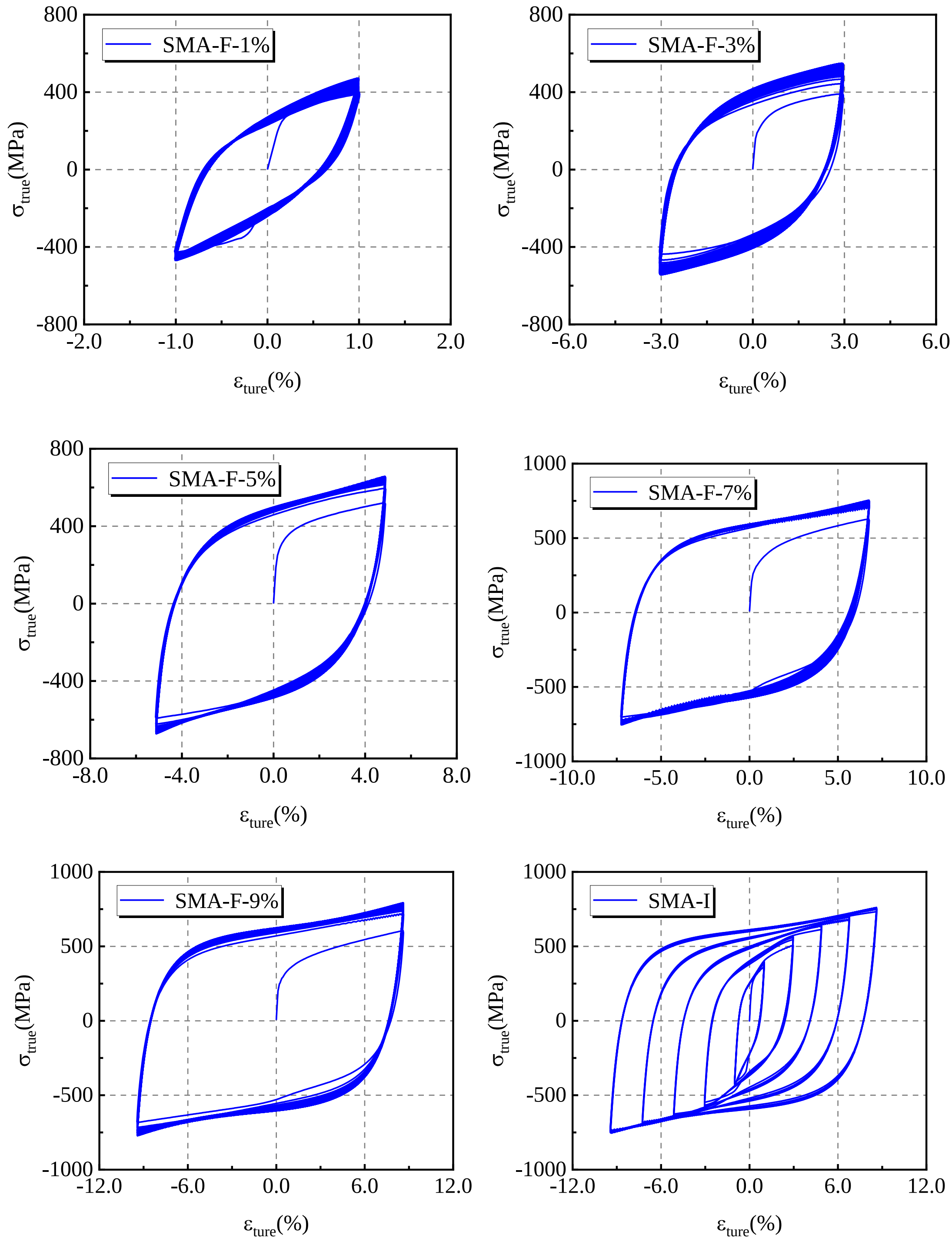

Fig. 3 Stress-strain curves of Fe-SMA material test specimens

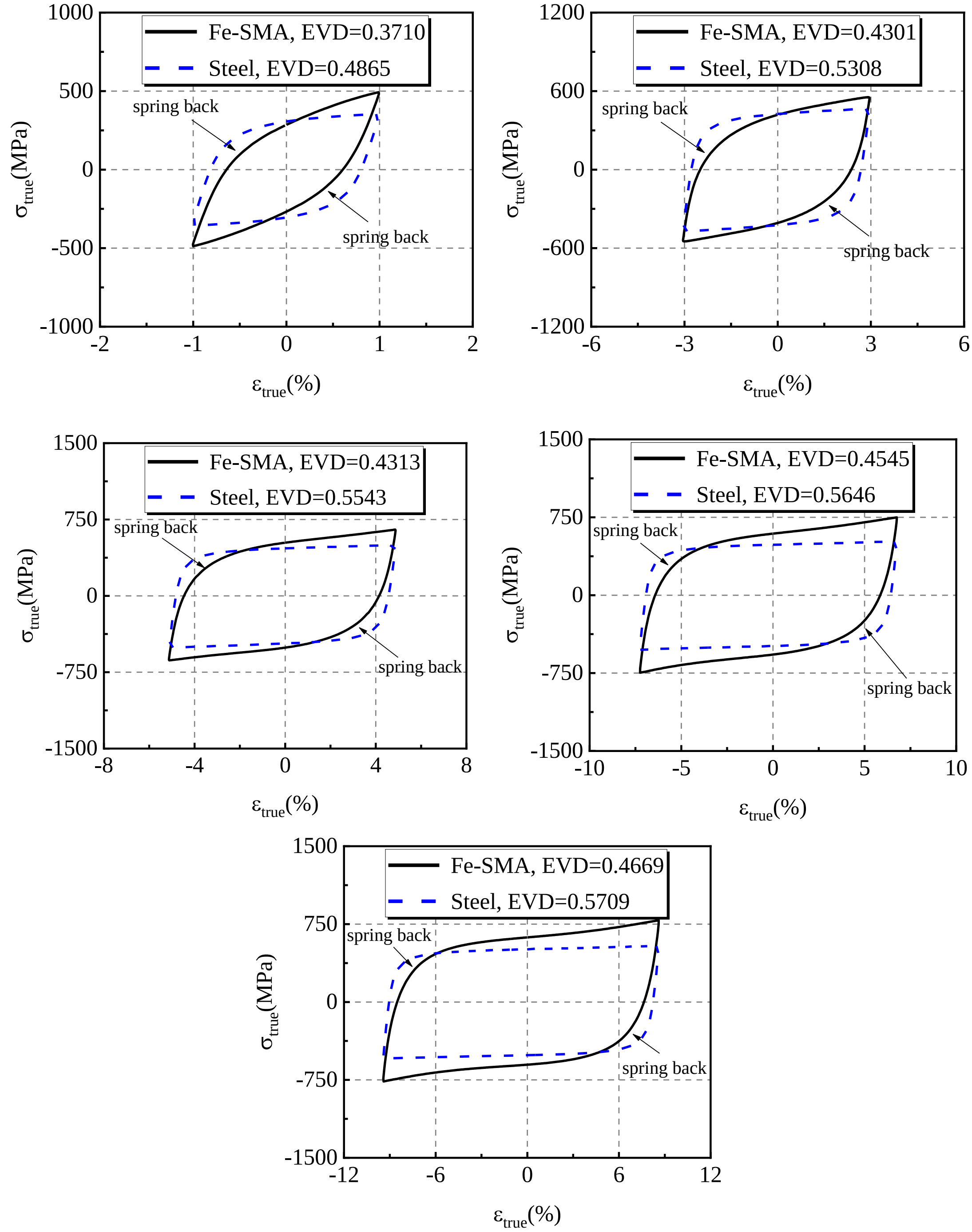

Fig. 4 Comparison of half-life hysteretic response between Fe-SMA and steel specimens

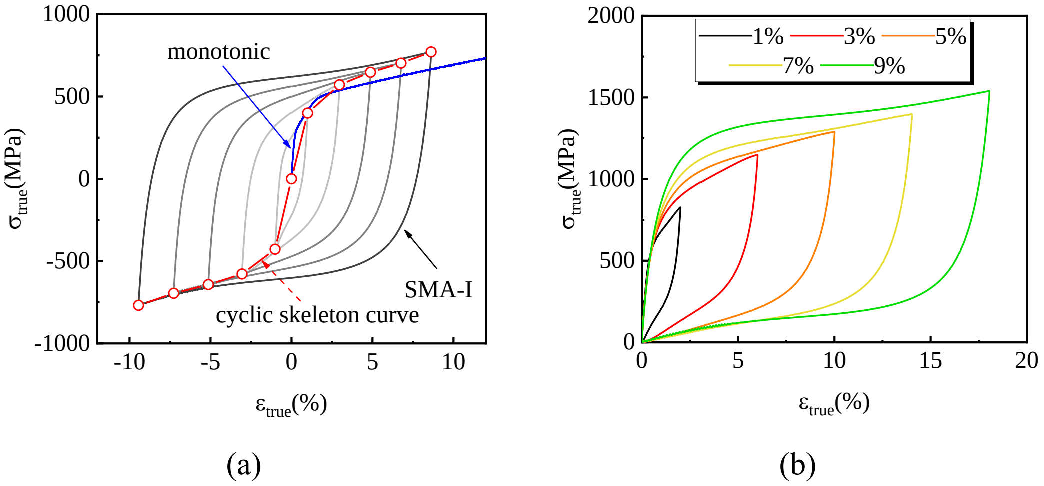

Fig. 5 Cyclic behavior of Fe-SMA: a) cyclic and monotonic stress-strain curves, b) non-Masing behavior of Fe-SMA

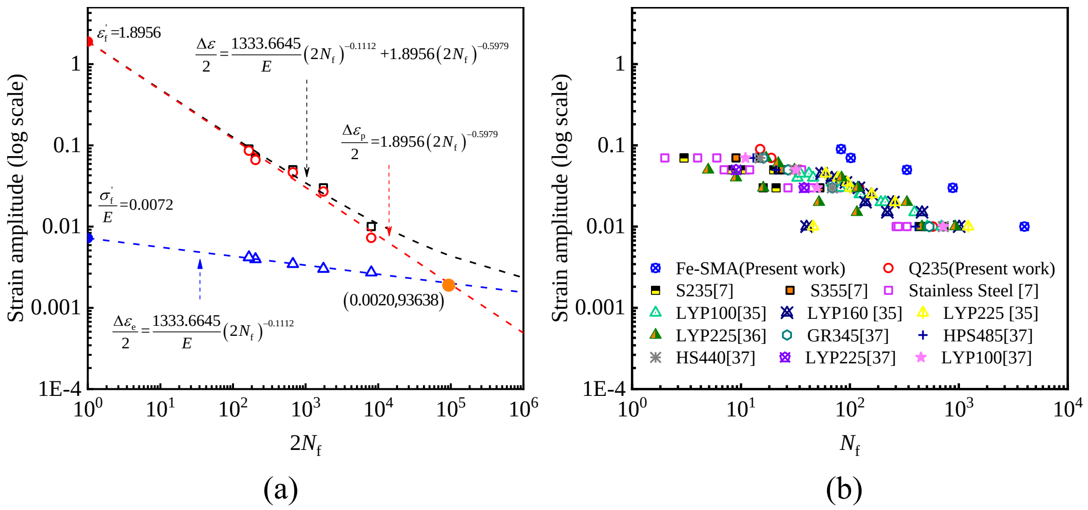

Fig. 6 Strain amplitude vs. fatigue life relationships: a) fitted curves for Fe-SMA, b) comparison with other materials

(a) (b)

Fig. 7 Macroscopic visual observation of fractured section: a) SMA-F-1%, SMA-F-9%

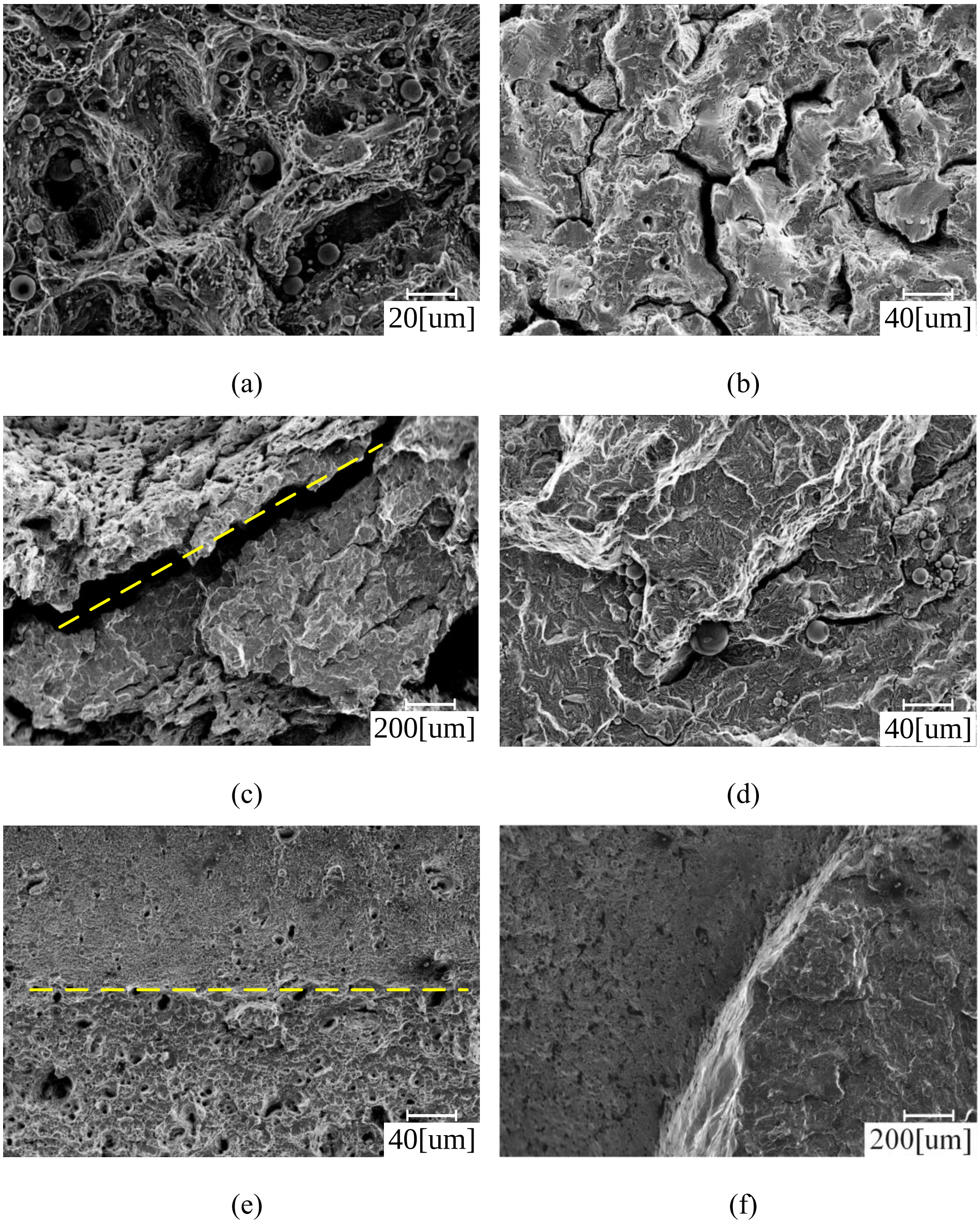

Fig. 8 Microscopic fractographic observation of fracture surface characterized by SEM

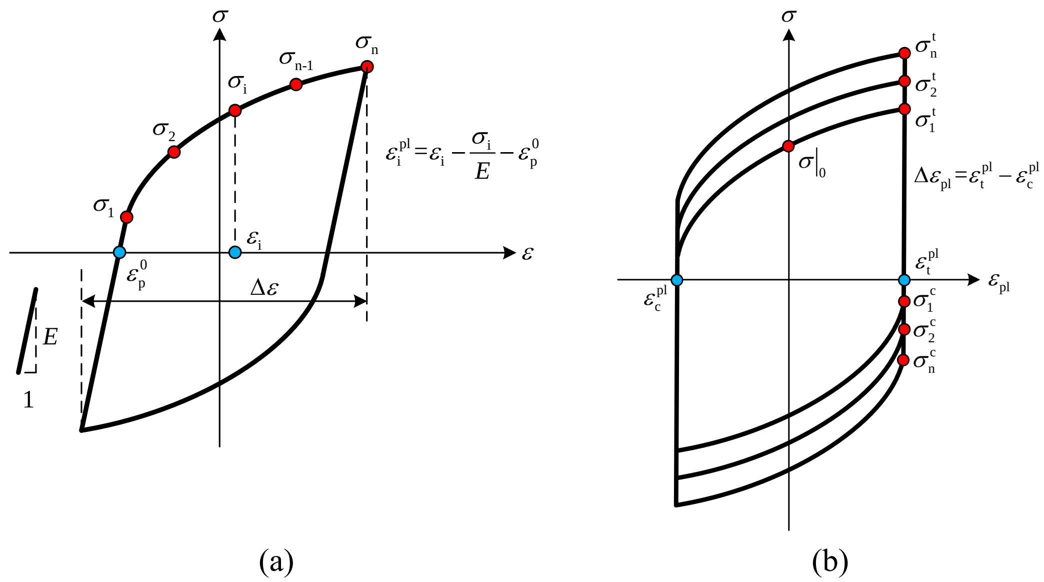

Fig. 9 Calibration of combined hardening material model parameters: a) kinematic hardening, b) isotropic hardening

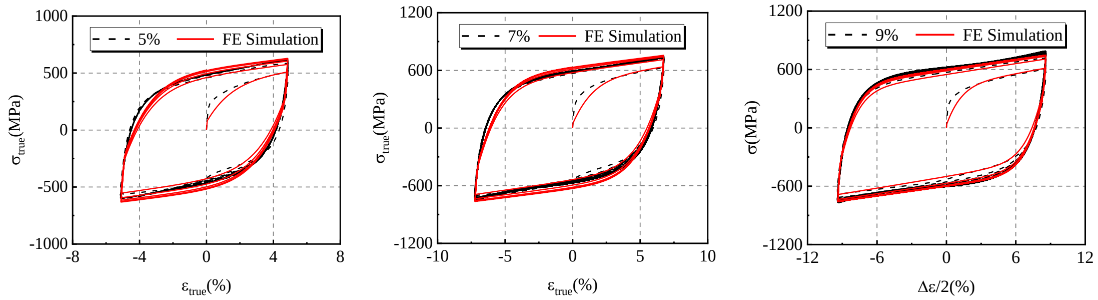

Fig. 10 Typical experimental and FE simulated stress-strain relationship of Fe-SMA

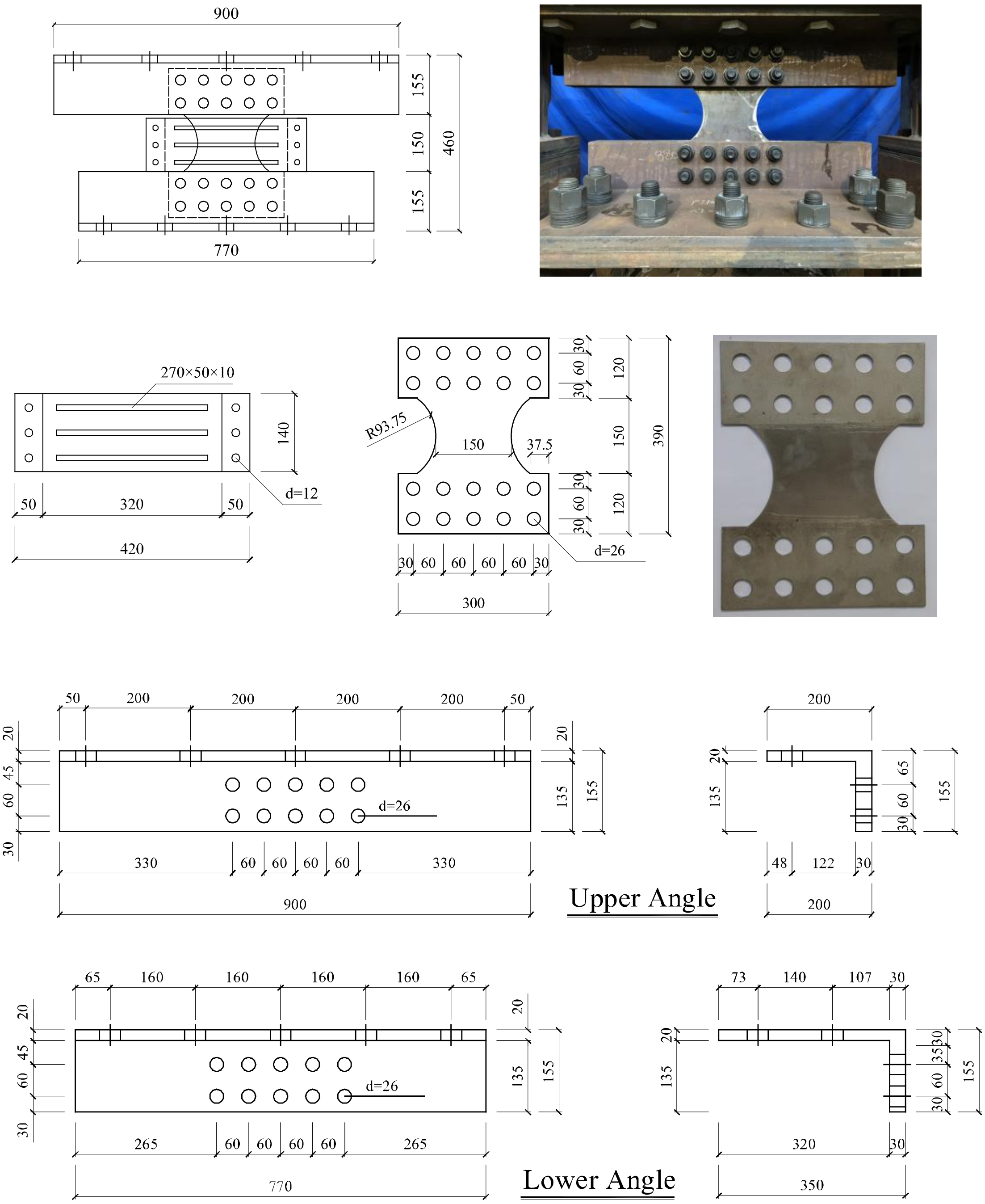

Fig. 11 Details of shear panel damper specimens

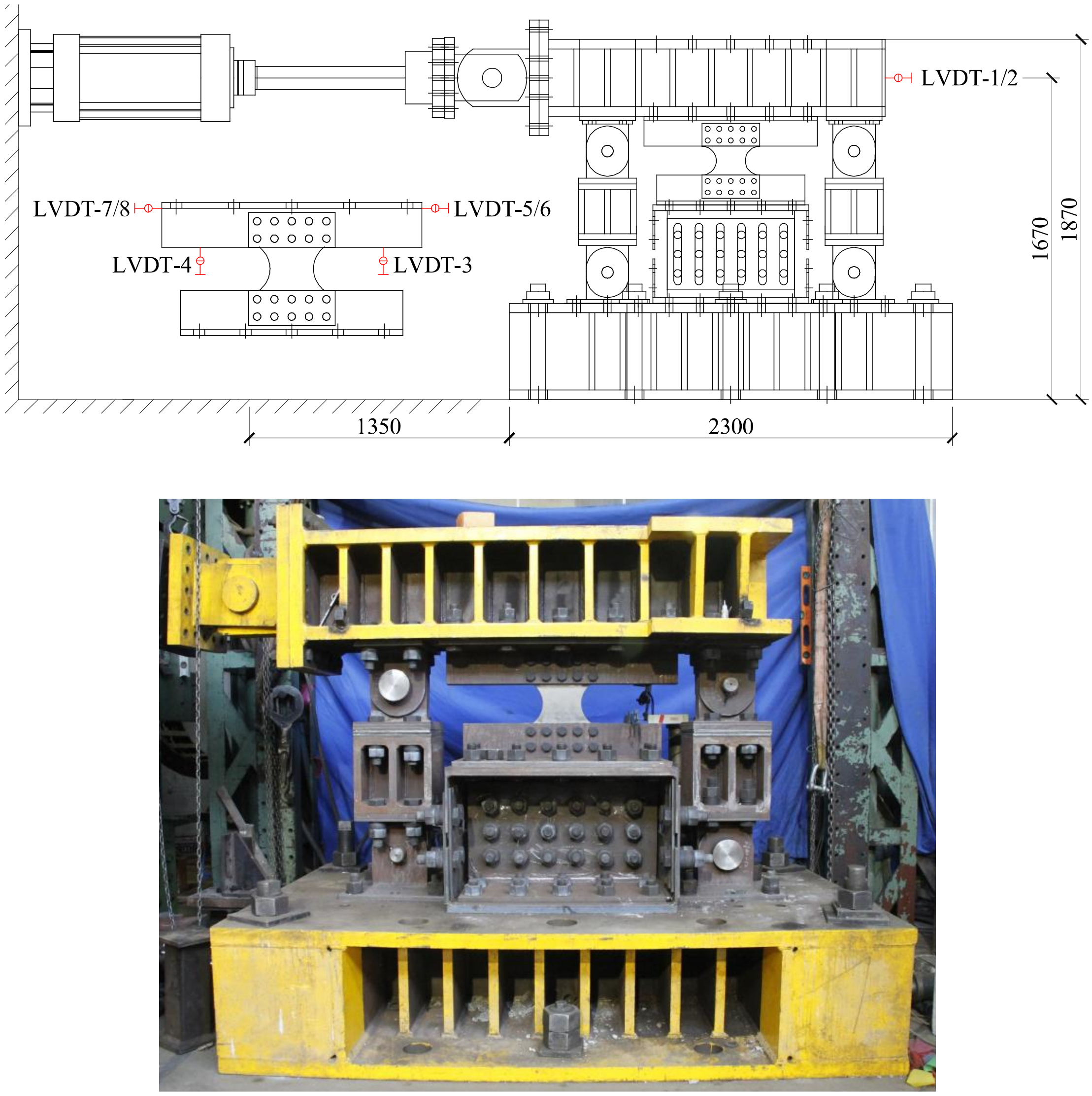

Fig. 12 Details of test setup and instrumentation

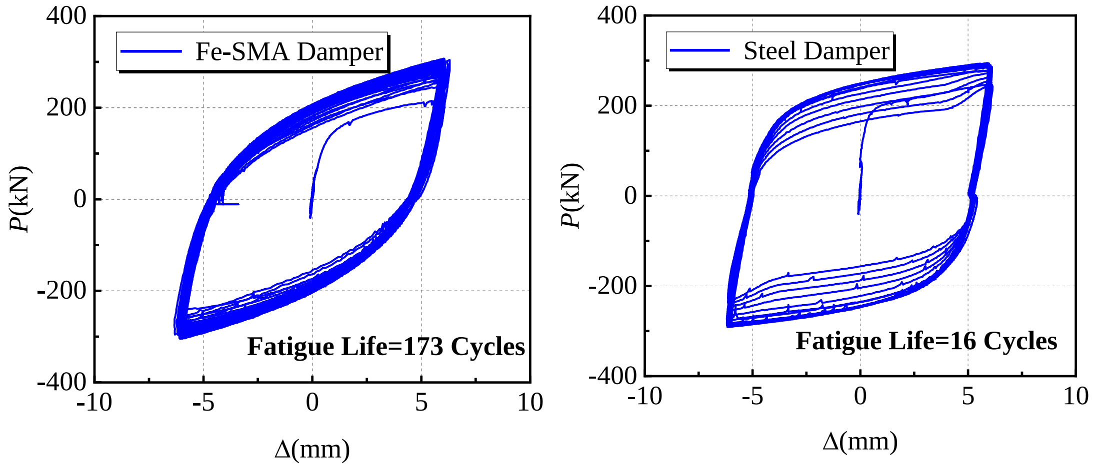

Fig. 13 Hysteretic behavior of damper specimens

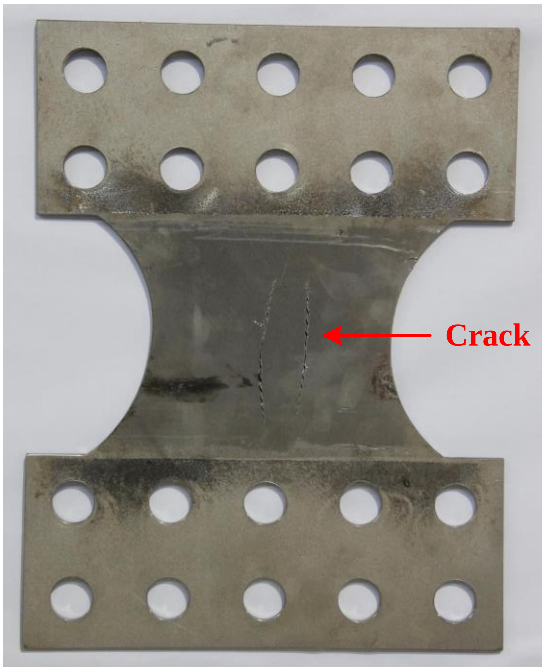

(a)

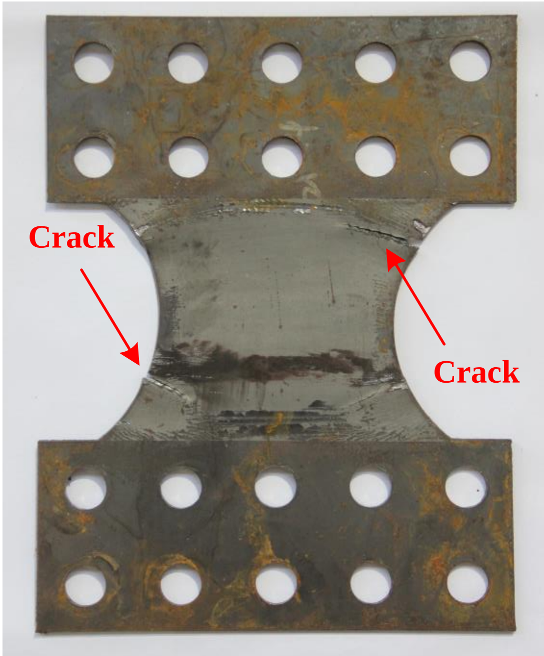

(b)

Fig. 14 Failure modes of damper specimens: a) Fe-SMA damper, b) steel damper

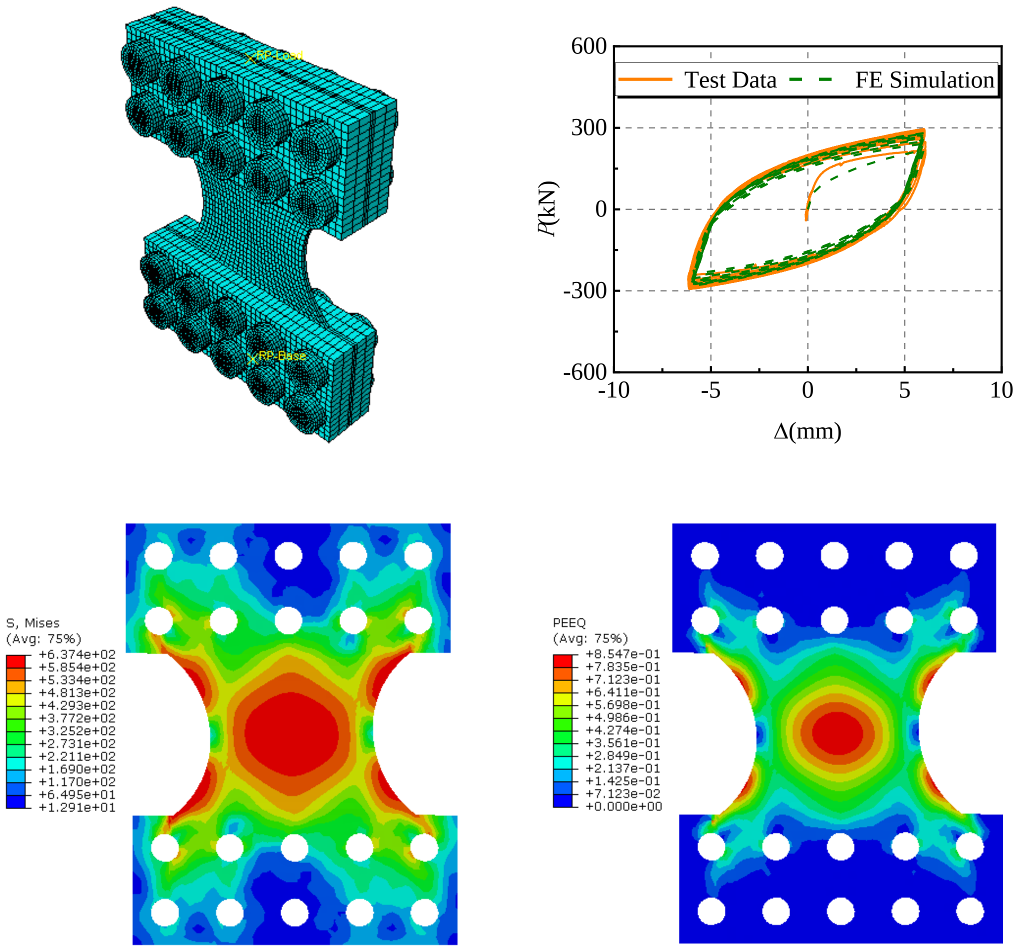

Fig. 15 Numerical simulation of Fe-SMA damper specimen